ACS NANO
Cite This: ACS Nano 2019, 13, 4191−4198
www.acsnano.org

ARTICLE

Dual-Phase Super-Strong and Elastic Ceramic

Fengshi Li,[†] Hewei Zhao,[†] Yonghai Yue,*[,†] Zhao Yang,[†] Youwei Zhang,[†] and Lin Guo*[,†,‡]

[†]School of Chemistry and Environment, Beihang University, Beijing 100191, P. R. China

[‡]State Key Laboratory for Modification of Chemical Fibers and Polymer Materials, Donghua University, Shanghai 201620, P. R. China

Supporting Information

ABSTRACT: **Ceramic materials exhibit very high stiffness and extraordinary strength, but they typically suffer from brittleness. Amorphization and size confinement are commonly used to reinforce materials. However, the inverse Hall−Petch effect and the shear-band softening effect usually limit further improvement of their performance under a critical size. With an optimum structure design, we demonstrate that dual-phase zirconia nanowires (DP-ZrO_2 NWs) with nanocrystals embedded in an amorphous matrix as a strengthening phase can overcome these problems simultaneously. As a result of this structure, *in situ* tensile tests demonstrate that the mechanical properties have been enormously improved in a way that does not follow both the inverse Hall−Petch effect and the shear band softening effect. The elastic strain approaches ~7%, and the ultimate strength is 3.52 GPa, accompanied by a high toughness of ~151 MJ m^{-3}, making the DP-ZrO_2 NW composite the strongest and toughest ZrO_2 ever achieved. The findings provide a way to improve the mechanical properties of ceramics in a controllable manner, which may serve as a pervasive approach to be broadly applied to a variety of materials.**

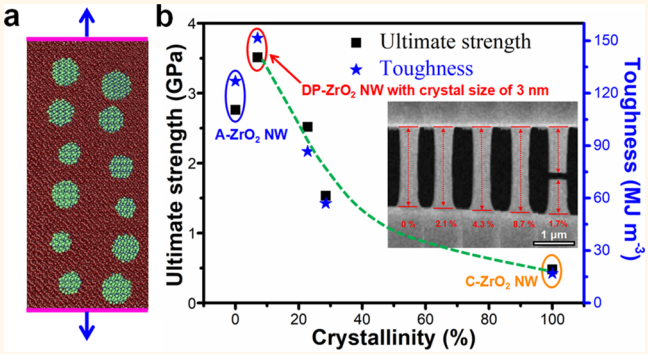

KEYWORDS: *dual-phase, zirconia nanowires, in situ tensile tests, inverse Hall−Petch effect, shear band softening effect*

Except for the rare and exorbitant diamond, widespread and low-cost ceramics are the hardest and strongest compression materials in the world due to their ultrastrong covalent bonds between atoms,[1,2] leading to wide applications in human society since the Neolithic age. However, the ultrastrong covalent bonds usually make ceramics extremely brittle in shearing and tension, which strongly restricts their applications in modern society. Softening the tone of the role of covalent bonds is very difficult.[3] How to make elastic and tough ceramics without sacrificing their high hardness is a worldwide problem and has always attracted scientists' interests. Throughout the development of ceramic materials, ceramics have usually been composed of soft materials such as a poly(lactic acid)/hydroxyapatite (PLA/HA) composite material[4] to overcome their brittle behavior. Indeed, the elasticity and toughness of ceramic materials are improved using the compositing method, but their hardness and strength are sharply decreased. Improving the intrinsic strength and toughness of ceramic materials simultaneously without compositing still poses an enormous challenge.

Recently, amorphization has been demonstrated as an efficient way to realize an ultrahigh strength that is much higher than that of the crystalline counterparts.[5−9] One example is bulk metallic glass (BMG), such as Co-, Fe-, Ni-, and Al-based BMG.[10] Owing to the lack of grain boundaries and dislocations,[11] the internal "defects" or inherently more fertile sites in the amorphous structure are favorable for shear transformations,[12] which renders the deformation mode of amorphous materials shear-band-dominated. Although the shear-band softening effect contributes to high strength of amorphous materials, it also restricts amorphous materials' toughness and elastic strain limit.[13,14] On the contrary, the toughness and elastic strain are considered to be affected by size confinement as well.[7,15] When the size is reduced to nanoscale, the maximum strain of metallic glasses approaches ~6%.[16] Structure design is another effective way to improve the mechanical properties of materials.[17] Usually, controlling the micromorphology and introducing obstacles, such as solid solution phase, precipitation, grain and twin boundaries, or even high dislocation density, can help to reach the theoretical strength and elastic strain limits simultaneously.[18−21] Recently, we have successfully synthesized a kind of fiber formed by superaligned *sub*-1 nm amorphous nanowires (NWs) and demonstrated that they have excellent mechanical properties.[22] The ultraslender NW morphology plays an important role in

Received: December 4, 2018
Accepted: January 29, 2019
Published: January 29, 2019

DOI: 10.1021/acsnano.8b09195
ACS Nano 2019, 13, 4191−4198

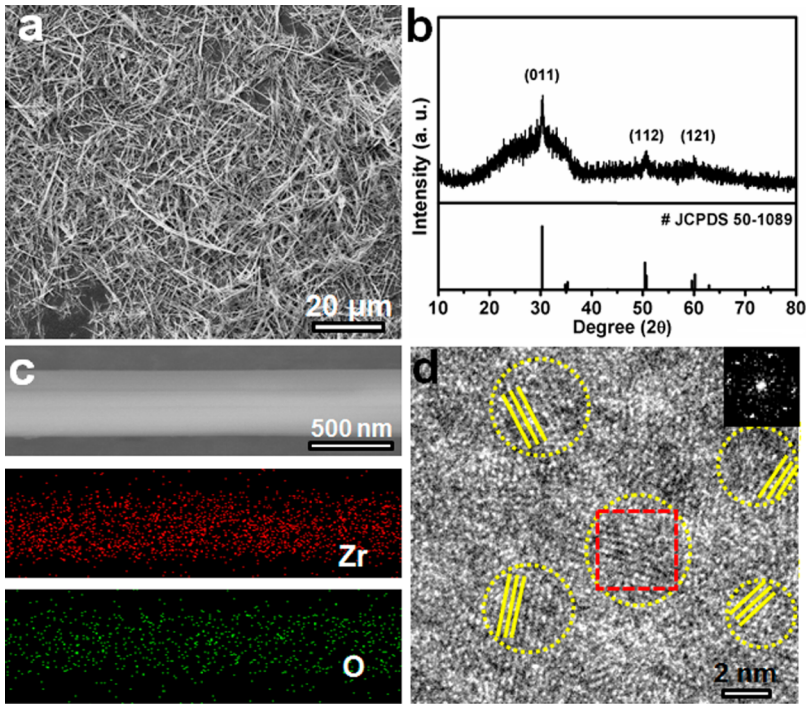

Figure 1. Characterization of DP-ZrO_2 NWs. (a) Low-magnification SEM image of the DP-ZrO_2 NWs. (b) XRD patterns of DP-ZrO_2. (c) EDS mapping of a single DP-ZrO_2 NW showing that Zr and O elements are fully and evenly distributed. (d) HRTEM image taken from a cross-sectional sample of DP-ZrO_2 NW. The inset is the corresponding FFT image taken from the red dashed frame.

inhibiting the shear-band softening effect. Furthermore, introducing nanocrystals into the amorphous matrix has also been proven to be an effective method to strengthen bulk materials. Thus combining structure design and crystal obstacles with size confinement in amorphous materials would be a marvelous strategy for further improving the mechanical properties of ceramics, which may break both the inverse Hall–Petch effect and the shear-band softening effect simultaneously and generate a synchronous improvement of strength and toughness.

Here we systematically study the method of strengthening and toughening the zirconia ceramic without compositing. We synthesized amorphous ZrO_2 NWs (without stabilizer) with diameter of ∼400 nm through a simple chemical route. By precisely controlling heat treatment, stable tetragonal structural ultrafine nanocrystals with a size of ∼3 nm were successfully introduced as a strengthening phase to form a kind of amorphous/nanocrystalline DP-ZrO_2 NW. *In situ* tensile tests in scanning electron microscopy (SEM) show that the ultimate strength of the DP-ZrO_2 NWs approaches ∼3.52 GPa with an ultrahigh elastic strain of ∼7% and a toughness of ∼151 MJ m^{-3}, making the DP-ZrO_2 NW composite the strongest and toughest ZrO_2 ever achieved. Besides, the strength of DP-ZrO_2 NWs is 1.3 times higher than that of amorphous zirconia NWs (A-ZrO_2 NWs) and 7 times higher than that of crystalline zirconia NWs (C-ZrO_2 NWs). An optimal balance between strength and toughness is therefore reached in the DP-ZrO_2 NWs, which will offer guidance to strengthen other amorphous nanomaterials.

RESULTS AND DISCUSSION

As a widely used material in many fields, such as refractory materials, pigments, wear-resistant materials, and piezoelectric materials, zirconia has attracted increasing attention recently.[23] The weakness in shearing and tension due to its poor toughness has dramatically restricted its applications. Garvie first proposed a toughening mechanism based on the phase-transition-induced volume effect in 1975.[24] However, the volume change induced by the phase transition can easily result in cracking. Meanwhile, it is also difficult to prepare pure and stable tetragonal zirconia above ∼30 nm in diameter at room temperature without other components (such as CaO, MgO, Y_2O_3, and CeO_2).[25,26] Therefore, it is important to develop a kind of zirconia material with both outstanding strength and toughness. Using a modified method of heating an alcohol–water $ZrOCl_2{\cdot}8H_2O$ solution (Supporting Information, Figure S1), a kind of 1D Zr-based NWs was successfully synthesized, followed by heat treatment at 700 °C to acquire pure 1D ZrO_2 NWs (Figure S2). The pure tetragonal crystalline feature of ZrO_2 (C-ZrO_2 NWs) was first confirmed by X-ray diffraction (XRD) (see more details in Figure S3, the blue spectrum), whereas its pure amorphous counterpart was obtained by precisely controlling the heating temperature to 300 °C (Figure S4a and the black XRD spectrum in Figure S3). To introduce ultrafine nanocrystals into the amorphous matrix, the temperature was then adjusted to 400 °C for 2 h. SEM and transmission electron microscopy (TEM) images (Figure 1a and Figure S4b) show a successful preparation of dual-phase 1D NWs with appearance similar to that of as-prepared samples. Moreover, random ultrafine tetrahedral ZrO_2 crystals distributed in the amorphous matrix have been defined by XRD (corresponding to JCPDS 50-1089, Figure 1b and Figure S3). The energy-dispersive spectroscopy (EDS) data collected from a single DP-ZrO_2 NW (Figure 1c) demonstrate that both the Zr and O were distributed uniformly in the NW without element segregation. The high-resolution transmission electron microscopy (HRTEM) image of this sample (Figure 1d) and its fast Fourier transform (FFT)

DOI: 10.1021/acsnano.8b09195
ACS Nano 2019, 13, 4191–4198

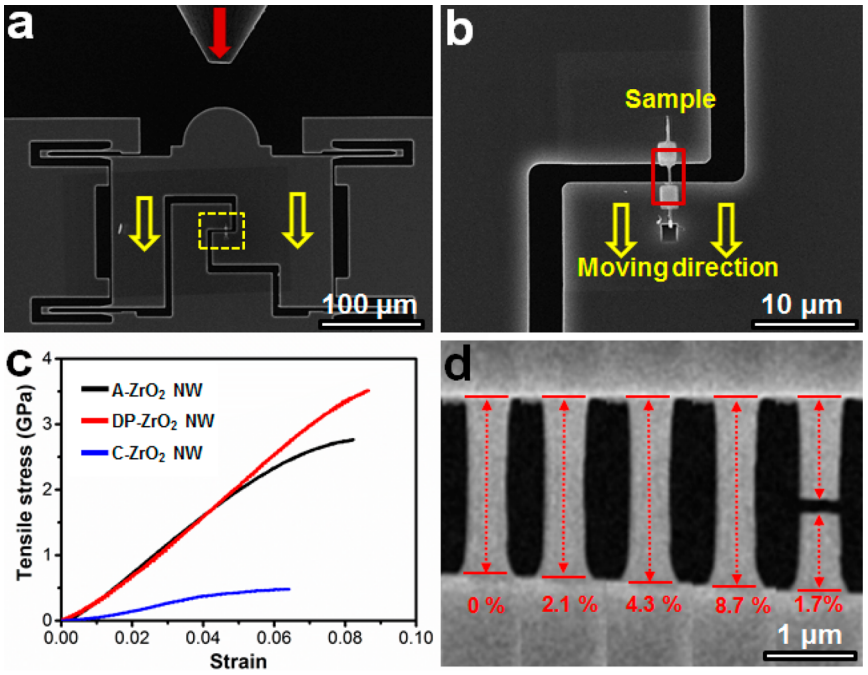

Figure 2. Experimental configuration and *in situ* SEM tensile tests. (a) Low-magnification SEM image and (b) high-magnification SEM image showing the experimental setup including the sample and the loading direction. (c) Stress−strain curves of the A-, DP-, and C-ZrO_2 NWs. (d) Snapshots extracted from Movie S1 showing the tensile process of a single DP-ZrO_2 NW with diameter of ∼380 nm.

image (inset in Figure 1d) further confirm its dual-phase structure. In addition, the HRTEM image also shows that the diameter of the random distributed ultrafine nanocrystals is ∼3 nm (Figure S5a). To study the size effect on the mechanical property, a series of DP-ZrO_2 NWs with different grain sizes were prepared (Figure S5). XRD patterns in Figure S3 show a trend of gradual increase in crystallinity as the heating temperature increases, and a pure crystalline structure is finally formed at 700 °C. All diffraction peaks for the samples treated at 400, 450, 500, and 700 °C can be indexed to the tetragonal ZrO_2, indicating its structural stability, which demonstrates that size confinement promotes the stabilization of the tetragonal ZrO_2 at room temperature.

In situ tensile tests were then conducted to study the mechanical properties of these three kinds of ZrO_2 NWs (A-, C-, and DP-ZrO_2 NWs) to reveal the strengthening mechanisms and the effect of grain size on mechanical properties. The uniaxial tensile tests were performed using an *in situ* quantitative nanoindenter (Hysitron Pi-85) inside an FEI Quanta 250 FEG SEM. The basic configuration of the tensile tests is presented in Figure 2a,b. After the 20 μm flat probe was positioned to touch the semicircular end of the particular push-to-pull (PTP) device, the indentation load could be converted to the yellow dashed line framed region in Figure 2a. Uniaxial tensile force was then loaded (along the direction marked by the two yellow arrows) to the tested ZrO_2 NW (red framed region in Figure 2b), which was fixed on the device by the focused ion beam (FIB) electron microscopy. Meanwhile, the force and displacement curve were recorded dynamically, and a real-time movie was also captured. The true force versus displacement curve of a tested sample can be accurately extracted and transferred to stress−strain curves by removing the contribution from the free PTP device. (See Figure S6 for more details.) All corresponding stress−strain curves of these three types of ZrO_2 NWs with comparable diameters of ∼400 nm are presented in Figure 2c, where at least five samples for each type of material have been subjected to the tensile test to confirm the reproducibility. The yielding strength of the tetragonal C-ZrO_2 NW is ∼0.5 GPa, with an elastic strain limit of ∼4%. (The blue curve in Figure 2c and Figure S7 shows the *in situ* tensile process from Movie S2.) Amorphization plays an important role in strengthening materials, as shown in Figure 2c (the black curve in Figure 2c and Figure S8 shows the *in situ* tensile process of A-ZrO_2 NWs from Movie S3), where the ultimate strength is ∼2.76 GPa and the elastic strain limit is ∼5.6%. Additionally, the total strain is increased to ∼8.1%, and the plastic strain is ∼2.5%. Furthermore, the mechanical properties of DP-ZrO_2 NWs could be further strengthened by introducing ultrafine nanocrystals to the amorphous matrix, as shown in Figure 2c. The sample treated at 400 °C shows both the highest strength and strain, as denoted by the red line in Figure 2c, where the ultimate strength approaches ∼3.52 GPa, accompanied by a very high strain of ∼8.7%, in agreement with previous literature claiming that introducing ultrafine nanocrystals to bulk amorphous materials can largely enhance their mechanical properties.[17,27−29] The strength is approximately seven times higher than that of C-ZrO_2 NWs. Figure 2d shows the corresponding snapshots obtained from Movie S1, which provide more details of the tensile test of the single DP-ZrO_2 NW with a diameter of ∼380 nm. The elastic strain can be calculated precisely after fracture according to the following expression[30]

$$\varepsilon_{elastic} = \varepsilon_{total} - \varepsilon_{remain} \quad (1)$$

where ε_{total} is the total strain before fracture and ε_{remain} is the remaining stain (*i.e.*, the plastic strain). The $\varepsilon_{elastic}$ suggests the recoverable elastic strain applied to the NW, which is calculated to be 7%, which agrees with the result obtained from the linear region from the stress−strain curve (red curve in Figure 2c) yet is beyond all of the reported elastic strain

DOI: 10.1021/acsnano.8b09195
ACS Nano 2019, 13, 4191−4198

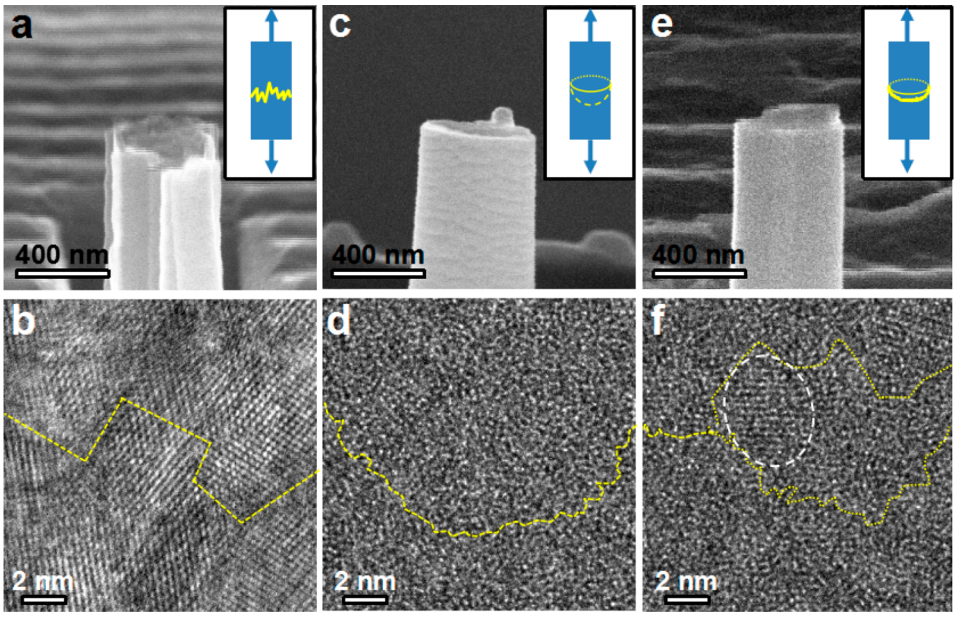

Figure 3. Fracture ends of these three typical ZrO_2 NWs and the corresponding sketch maps of the fracture mechanism. (a,b) Brittle fracture mode of C-ZrO_2 NWs. (c,d) Hypothetical shear band sliding mode of the A-ZrO_2 NWs. (e,f) Hypothetical micro shear band sliding and embryonic shear band generation mode of DP-ZrO_2 NWs. White dashed ellipse in panel f locates a small grain.

limits of metallic materials.[20] To further confirm whether the deformation is fully elastic, we conducted repeated loading–unloading tests with the same strain rate ($\sim 2.5 \times 10^{-3}$ s^{-1}) and full unloading in each cycle. Figure S9 shows cyclic test and the stress–strain curve taken from the loading–unloading test of another single DP-ZrO_2 NW. After a strain value of up to ~6.5% was experienced during the third cycle, the DP-ZrO_2 NW could still recover its original length. However, a slight plastic deformation happened during the fourth cycle, and a slight change of the slope could be observed when the strain exceeded 6.5% (Figure S9). The calculated Young's moduli for the DP-ZrO_2 NW in Figure 2c and Figure S9 are ~43 and 34 GPa, lower than the values reported for the bulk ZrO_2, making our DP-ZrO_2 NW a kind of ceramic material with high strength but low modulus. Furthermore, we observe that the deformation is uniform, with no obvious macro shear bands, which is attributed to the inhibition by size confinement. The introduction of ultrafine crystals indeed largely strengthens the pure amorphous structure as designed but reduces the plasticity slightly (1.7% plastic strain for the DP-ZrO_2 NW and 2.5% plastic strain for the A-ZrO_2 NW).

To further clarify the deformation mechanisms, the fracture ends of three kinds of NWs (A-, C-, and DP-ZrO_2 NWs) were also studied. Figure 3a shows a fracture end of a single C-ZrO_2 NW, which exhibits an irregular fracture surface, similar to the feature of brittle fracture. The typical roughness induced by grain boundaries can be observed after the catastrophic fracture, which is in accordance with the lowest plasticity for the C-ZrO_2 NWs. Interjunctions of free surface and grain boundaries will serve as dislocation sources where the dislocations pile up, and a crack would first occur, followed by propagation along the grain boundaries (yellow line in Figure 3b) and the generation of an irregular fracture surface (Figure 3a). Figure 3c shows a typical fracture end of the A-ZrO_2 NWs. The deformation mechanism of the amorphous material changes completely from that of its crystalline counterparts by shifting from a dislocation-activated mode to the activation of shear bands.[12] The high elastic strain in amorphous materials originates from the coupling of elastic elongation of bonds and changes in the bond-angle distribution[27] rather than from the recoverable lattice spacing elongation only.[19,21] No obvious shear bands and necking occurred during the tensile test, as shown in Figure S8. The uniform deformation indicates an effective suppression of macro shear band formation induced by the reduction of the specimen size.[15,27−29] Another reason why there is no obvious necking is due to the high strain rate (2.5×10^{-3} s^{-1}), which is higher than the strain rate for necking formation.[30] As the force increases beyond the yield point, the NW shows damage mainly in the form of micro shear bands, resulting in a dimple-like fracture end, as shown in Figure 3c. (A hypothetical curved fracture track is denoted by the yellow curved line in Figure 3d.)[31] The difference in chemical bonding between crystalline and amorphous structural ZrO_2 NWs was examined by X-ray photoelectron spectroscopy (XPS) to further reveal the different deformation mechanisms between the C-ZrO_2 NWs and A-ZrO_2 NWs. Figure S10a,b shows the spectrum for the Zr 3d and O 1S states of A-ZrO_2 NWs, and Figure S10c,d shows the corresponding spectrum for C-ZrO_2 NWs. The reduced state of amorphous zirconium element is traditionally considered to be the result of electron transfer from oxygen to zirconium, thereby leading to electron gain. However, the binding energy of the oxygen core for the A-ZrO_2 NWs also shows a 0.1 to 0.3 eV shift to lower values, which also means that the oxygen element shows a reduced (electron gain) state instead of the oxidized (electron loss) state. The XPS spectrum reveals that the chemical bond between zirconium and oxygen atoms in A-ZrO_2 NWs is of more ionic bonding than that in C-ZrO_2. Thus a larger force is needed to break the chemical bond of the A-ZrO_2 than its crystalline counterpart. Furthermore, the amorphous structure can be taken as a mixture consisting of atomic clusters and open volume regions,[29] and a large amount of free-volume content can strongly enhance both the atomic jump and shear transformation zones,[6,32] resulting in an

DOI: 10.1021/acsnano.8b09195
ACS Nano 2019, 13, 4191−4198

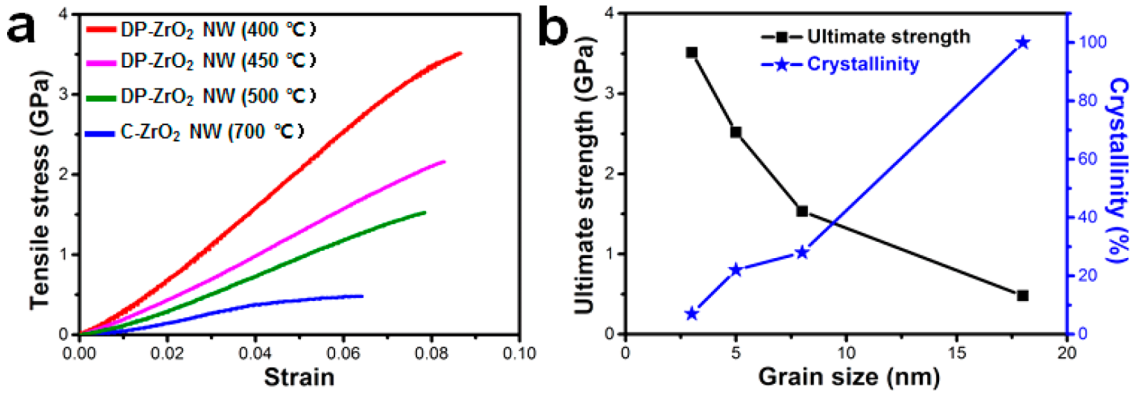

Figure 4. Strong size effect on the strength of DP-ZrO_2 NWs with different crystallinities. (a) Stress−strain curves for the ZrO_2 NWs with different crystal sizes and crystallinities. (b) Size and crystallinity dependence of the ultimate strength of the DP-ZrO_2 NWs.

enhancement of the deformation ability, which may be the origin of the excellent plasticity of A-ZrO_2 NWs.

To inhibit the shear-band softening effect,[9] the heat treatment condition was well adjusted to produce DP-ZrO_2 with an amorphous/nanocrystalline dual-phase structure (as shown in Figure 1d and Figure S4b−d). The distributed nanocrystals in the amorphous matrix could restrict the stable generation of localized shear bands as well as the spread of the shear bands (Figure 3e,f), resulting in a dramatic increase in the strength of the DP-ZrO_2 NWs, which is even better than that of A-ZrO_2 NWs. The yielding strength increases by 50% (3.0 GPa for DP-ZrO_2 NWs treated at 400 °C and ∼2 GPa for A-ZrO_2 NWs) and achieves an ultimate strength of ∼3.52 GPa. Figure 3e,f shows the typical fracture ends of the DP-ZrO_2 NW, where one can note that the dimple-like fracture feature is not as obvious as that of A-ZrO_2 NW shown in Figure 3c, which is due to the restriction effect induced by the ultrafine crystals in the DP-ZrO_2 NWs. When increasing the temperature from 400 to 450 °C, the size of the crystals is first increased from ∼3 to ∼5 nm with improved crystallinity, then to ∼8 nm in DP-ZrO_2 NWs at 500 °C (Figures S4d and S5c), and finally reaches ∼18 nm in C-ZrO_2 NWs at 700 °C (Figures S2d and S5d). The crystallinity can be roughly speculated from the XRD results, which are taken under same testing conditions for these DP- and C-ZrO_2 NWs. It is speculated to be ∼7% for the DP-ZrO_2 NWs treated at 400 °C, ∼22.8 and ∼28.5% for the DP-ZrO_2 NWs treated at 450 and 500 °C, respectively, and 100% for the C-ZrO_2 NWs treated at 700 °C. (See more details in Figure S11 and Table S1.) The strength has a strong size effect for these NWs with similar diameter.

Figure 4a shows the stress−strain curves for all types of NWs contain crystals, where it is only 0.5 GPa for the C-ZrO_2 NWs with crystal size >18 nm (the blue curve in Figure 4a). As the crystals size decreases and the amorphous structure is introduced, the strength is increased to 1.5 GPa for the DP-ZrO_2 NWs (treated at 500 °C, the green curve in Figure 4a) with a crystal size of 8 nm and a crystallinity of 28%. When slightly decreasing the temperature to 450 °C, the DP-ZrO_2 NWs show a crystallinity of 22% together with a lower crystal size (∼5 nm), which leads to a continuous increase in the strength (2.52 GPa, the pink curve in Figure 4a). However, the inverse Hall−Petch does not occur, and the strength keeps increasing as the crystal size decreases, as shown in Figure 4b. For the DP-ZrO_2 NWs with a crystal size decreasing to 3 nm and a crystallinity of 7% (treated at 400 °C), the amorphous matrix plays an important role in contributing to both the high strength and the ultrahigh elastic strain limit. If the NW structure is purely crystalline with a crystal size below 8 nm, then grain rotation and grain boundary sliding take the place of dislocation behavior, leading to an inverse Hall−Petch effect.[8,9] Unlike the crystalline materials, there is no slipping system out of crystals for dislocations. The detrimental influence of the inverse Hall−Petch effect has been successfully mitigated through this dual-phase structure. A strong size effect on the stress has been revealed, even though the crystal size is extremely small (3 nm). In addition to the size effect, an inverse crystallinity effect on the stress is also demonstrated, as shown in Figure 4b. Here the amorphous nature plays an important role in the strengthening mechanism.

For crystals with a size >8 nm, there would be a small amount of preexisting dislocations in these crystals, and the stress needed to start the motivation of these preexisting dislocation is low, resulting in a relative low strength. Moreover, for large crystals, the crystallinity is high, which means that the ratio of the amorphous phase is low and the thickness of the amorphous phase surrounding crystals is thinner, leading to a poor ability to absorb and impede dislocation motivation. The dislocations then have opportunities to cross the thin amorphous layers to other crystals, finally decreasing the strength. An extreme example is the pure polycrystalline materials. Traditional theory considers the grain boundaries as a kind of thin amorphous materials. When we lower the crystallinity, the ratio of the amorphous phase is increased, which is accompanied by a decrease in the crystal size. There are nearly no preexisting dislocations in such small crystals with a size <8 nm, and amorphous surroundings can act as a cleaner to absorb the dislocation easily even if there are several sporadic dislocations. The thickness of the amorphous is increased and would be a cleaner and terminator to dislocations. In addition, the XPS results in Figure S10 suggest the chemical bond between zirconium and oxygen atoms for A-ZrO_2 NWs. The yielding should first occur in crystalline phase, but the stress needed to emit new dislocations is much higher than the stress needed to trigger the preexisting dislocations. Furthermore, the ability to absorb and impede dislocation motivation is also increased with the increase in the thickness of amorphous. Dislocations would be emitted from the crystal/amorphous interface and propagate across the whole crystal, but they would be inhibited when meeting the opposite interface and sinking into the amorphous phase, leading to a continuous increase in strength (Figures 2c and 4a). Moreover, nonuniformly distributed nanocrystals in the amorphous

DOI: 10.1021/acsnano.8b09195
ACS Nano 2019, 13, 4191−4198

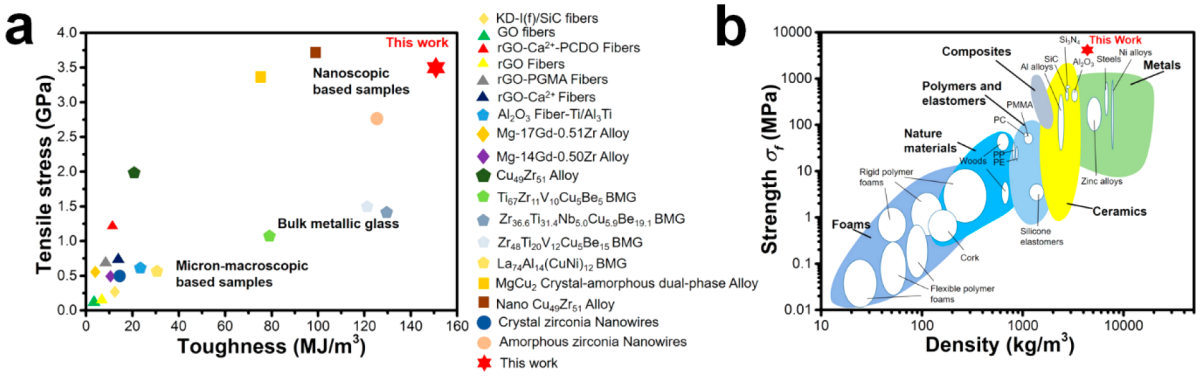

Figure 5. Comparison of these related materials' performances. (a) Comparison of the stress and toughness for the nanobased and microbased samples. (b) Comparison of the strength and density between our materials and other traditional materials.

matrix and an incontrollable volume fraction of nanocrystals can restrict the stable generation of embryonic shear bands. The embedded crystals divide and rotate within any shear bands, which need much higher stress to happen, contributing to the hardening as well and conquering the softening effect of the shear band. Grain sliding and rotation would happen only if the stress is high enough to break the amorphous surrounding environments. The shear band would be blocked when it contacts nanocrystal (marked by the white dashed circle in Figure 3f) and would then be divided into multiple embryonic shear bands. The shear-band softening effect is also effectively inhibited due to the introduction of ultrafine crystals. The highest elastic strain for the DP-ZrO_2 NWs approaches 7% (DP-ZrO_2 NWs treated at 400 °C), making our strategy an effective method to strengthen 1D amorphous materials.

In addition to strength, toughness is another important parameter in the evaluation of the engineering materials. The toughness values of these three kinds of ZrO_2 NWs were calculated from the stress−strain curves (Figure S11 and Table S1). The calculated toughness of the C-ZrO_2 NW is only ∼17 MJ m^{-3}, with an ultimate strength of 0.5 GPa, yet after amorphization, both the ultimate strength and the toughness are increased dramatically for the A-ZrO_2 NW, reaching 2.76 GPa for the ultimate strength and ∼127 MJ m^{-3} for the toughness. As a combination of high strength and toughness, the DP-ZrO_2 NWs are considerably better than those of micro/nano-material-based fibers, especially for those treated at 400 °C, which have a toughness of ∼151 MJ m^{-3}, ∼9 times higher than that of the C-ZrO_2 NW and 1.2 times higher than those of the A-ZrO_2 NW. (See Table S1.) To demonstrate the advantage of the DP-ZrO_2 structure, a wide range of advanced fiber and alloy materials was investigated. The values of strength and toughness are compared with each other and summarized in Figure 5a. The ultimate strength and the toughness of DP-ZrO_2 NW are higher than those of most other micro/nano-material-based fibers.[33−42] Figure 5b shows the comparison between DP-ZrO_2 NWs and traditional materials such as metals, ceramics, composites, polymers, elastomers, nature materials, and foams. Impressively, the mechanical properties of our DP-ZrO_2 NWs are located in the upper right region, indicating a very high specific strength and toughness for our DP-ZrO_2 NWs, which demonstrates that our DP-ZrO_2 NWs are very strong, tough, and lightweight and are of a low modulus.

CONCLUSIONS

Using the chemical synthesis method and precise heat treatment, three types of ZrO_2 NWs (A-, DP-, and C-ZrO_2 NWs) have been successfully prepared. *In situ* tensile tests in SEM show that the DP-ZrO_2 NWs treated at 400 °C possess the most excellent mechanical properties via successfully mitigating both the shear-band softening effect and the inverse Hall−Petch effect by the controllable combination of amorphous and nanocrystalline structures. The highest elastic strain limit of the DP-ZrO_2 NW approaches ∼7%, making the DP-ZrO_2 NW the strongest zirconium dioxide with the highest ultimate strength (3.52 GPa), lowest modulus (34−43 GPa), and highest toughness (151 MJ m^{-3}) ever achieved. Although this dual-phase structural design was first realized in 1D nanomaterials, which has been proven to be an effective strategy to strengthen materials, our approach to prepare the dual-phase nanomaterials will be a universal method, which may dramatically broaden the range of applications in other types of brittle ceramic materials.

EXPERIMENTAL SECTION

Synthesis of ZrO_2 NWs. 0.7 g polyvinylpyrrolidone (PVP) was dissolved in a 60 mL solution of deionized water and ethanol at the ratio of 1:59, and the solution was dispersed by ultrasonication for 15 min. Then, zirconium oxychloride octahydrate (0.15 mmol) was added, and the solution was ultrasonicated for 30 min. This solution was then incubated at 30 °C for 2 h under vigorous stirring. The precipitate was collected after centrifugation and was carefully washed with deionized water to clean out the remnant salt and subsequently dried in a freeze dryer for 24 h. The as-prepared NWs were treated at different temperature in a muffle furnace to form different structural samples.

Characterization. The morphologies and structures of the NWs were observed by a JEOL 7500F SEM. The surface compositions were analyzed by EDS. The samples were dispersed on the Si platelet for the test. TEM and HRTEM images were obtained with a Cs-corrected Titan G2 TEM at an accelerating voltage of 300 kV. The phase structures were characterized by XRD (SHIMADZU XRD-6000) with the diffraction patterns collected on an XRD in the 10−80° (2θ) range with a scanning rate of 0.03 s^{-1}. All XPS results were performed with a Thermo Scientific Escalab 250Xi instrument by using a monochromatic Al KR X-ray source.

Tensile Test Operation. *In situ* tensile tests were conducted on a Pico Indenter 85 nanoindenter (Pi-85) coupled to a PTP device inside a Quanta 250 FEG SEM at 10 kV. The single NW was transferred and fixed onto the PTP device by the FIB. Calibration of the conductive diamond flat punch (20 μm in diameter) was performed and confirmed before every test. After the 20 μm flat probe was positioned to touch the semicircular end of the PTP device, the

DOI: 10.1021/acsnano.8b09195
ACS Nano 2019, 13, 4191−4198

ZrO_2 NW was pulled under a displacement control mode with a displacement rate of 5 nm s^{-1} until the sample fractured. During the tensile test, the force and displacement curve were recorded dynamically, and real-time video was also recorded.

Quantitative Analysis. To calculate the stress and strain on the tested single NWs, their initial length, cross-sectional area, and the force applied were determined. The initial length and diameter of every sample were determined using SEM images prior to the test. (The cross-section of the NW is assumed to be round.) The force in the raw force−distance curve was directly recorded including the contribution from both the sample and the PTP device. Thus the force applied on the sample can be accurately determined by subtracting the contribution of the PTP device. For every test, the stiffness of the PTP device was confirmed when the NW was totally fractured.

ASSOCIATED CONTENT

Supporting Information

The Supporting Information is available free of charge on the ACS Publications website at DOI: 10.1021/acsnano.8b09195.

Figures S1−S11 show SEM images of precursor zirconia; characterization of a single C-ZrO_2 NW; XRD curves of the corresponding samples; structure characterizations for A-, C-, and DP-ZrO_2 NWs; grain size distribution; load−displacement curve of the A-ZrO_2 NW; SEM images extracted from the recorded Movies S2 and S3; cyclic tensile test of a single DP-ZrO_2 NW; high-resolution XPS spectra of A-ZrO_2 NWs and the C-ZrO_2 NWs; and crystallinity effect on both the stress and toughness. Table S1. Mechanical properties data and the composition for different structures of ZrO_2 NWs (PDF)

Movie S1. *In situ* tensile tests of DP-ZrO_2 NWs under SEM observation (AVI)

Movie S2. *In situ* tensile tests of C-ZrO_2 NWs under SEM observation (AVI)

Movie S3. *In situ* tensile tests of A-ZrO_2 NWs under SEM observation (AVI)

AUTHOR INFORMATION

Corresponding Authors

*Y.Y.: E-mail: yueyonghai@buaa.edu.cn.

*L.G.: E-mail: guolin@buaa.edu.cn. Fax/Tel: +86-10-82338162.

ORCID

Fengshi Li: 0000-0002-6351-0417

Hewei Zhao: 0000-0001-8851-9920

Yonghai Yue: 0000-0002-8945-2032

Lin Guo: 0000-0002-6070-2384

Author Contributions

Y.Y. and L.G. proposed and supervised the project; F.L. and Y.Y. performed the *in situ* experiments; Y.Y. and Z.Y. performed the TEM characterization; F.L., H.Z., and Y.Z. prepared the sample; Y.Y., L.G., and F.L. analyzed data and wrote the manuscript. All authors participated in discussions of the research.

Notes

The authors declare no competing financial interest.

ACKNOWLEDGMENTS

We thank Prof. Nicholas A. Kotov for very helpful discussions. This study was supported by the National Natural Science Foundation of China (51532001, 51741201), the Fundamental Research Funds for the Central Universities (YWF-18-BJ-Y-56), and State Key Laboratory for Modification of Chemical Fibers and Polymer Materials of Donghua University.

REFERENCES

(1) Bouville, F.; Maire, E.; Meille, S.; Van de Moortèle, B.; Stevenson, A. J.; Deville, S. Strong, Tough and Stiff Bioinspired Ceramics from Brittle Constituents. *Nat. Mater.* **2014**, *13*, 508−514.

(2) Daniel, R.; Meindlhumer, M.; Baumegger, W.; Zalesak, J.; Sartory, B.; Burghammer, M.; Mitterer, C.; Keckes, J. Grain Boundary Design of Thin Films: Using Tilted Brittle Interfaces for Multiple Crack Deflection Toughening. *Acta Mater.* **2017**, *122*, 130−137.

(3) Derand, T.; Molin, M.; Kvam, K. Bond Strength of Composite Luting Cement to Zirconia Ceramic Surfaces. *Dent. Mater.* **2005**, *21*, 1158−1162.

(4) Sun, L.; Danoux, C. B.; Wang, Q.; Pereira, D.; Barata, D. B.; Zhang, J.; Lapointe, V.; Truckenmüller, R.; Bao, C.; Xu, X.; Habibovic, P. Independent Effects of the Chemical and Microstructural Surface Properties of Polymer/Ceramic Composites on Proliferation and Osteogenic Differentiation of Human MSCs. *Acta Biomater.* **2016**, *42*, 364−377.

(5) Wang, W. H. Correlations between Elastic Moduli and Properties in Bulk Metallic Glasses. *J. Appl. Phys.* **2006**, *99*, No. 093506.

(6) Schuh, C. A.; Hufnagel, T. C.; Ramamurty, U. Mechanical Behavior of Amorphous Alloys. *Acta Mater.* **2007**, *55*, 4067−4109.

(7) Zhang, H. T.; Tersoff, J.; Xu, S.; Chen, H. X.; Zhang, Q. B.; Zhang, K. L.; Yang, Y.; Lee, C.-S.; Tu, K.-N.; Li, J.; Lu, Y. Approaching the Ideal Elastic Strain Limit in Silicon Nanowires. *Sci. Adv.* **2016**, *2*, No. e1501382.

(8) Camposilvan, E.; Torrents, O.; Anglada, M. Small-Scale Mechanical Behavior of Zirconia. *Acta Mater.* **2014**, *80*, 239−249.

(9) Sun, B. A.; Wang, W. H. The Fracture of Bulk Metallic Glasses. *Prog. Mater. Sci.* **2015**, *74*, 211−307.

(10) Telford, M. The Case for Bulk Metallic Glass. *Mater. Today* **2004**, *7*, 36−43.

(11) Greer, A. L. Metallic Glasses. *Science* **1995**, *267*, 1947−1953.

(12) Shimizu, F.; Ogata, S.; Li, J. Yield Point of Metallic Glass. *Acta Mater.* **2006**, *54*, 4293−4298.

(13) Schiøtz, J.; Di Tolla, F. D.; Jacobsen, K. W. Softening of Nanocrystalline Metals at Very Small Grain Sizes. *Nature* **1998**, *391*, 561−563.

(14) Wang, L. H.; Teng, J.; Liu, P.; Hirata, A.; Ma, E.; Zhang, Z.; Chen, M. W.; Han, X. D. Grain Rotation Mediated by Grain Boundary Dislocations in Nanocrystalline Platinum. *Nat. Commun.* **2014**, *5*, 4402.

(15) Guo, H.; Yan, P. F.; Wang, Y. B.; Tan, J.; Zhang, Z. F.; Sui, M. L.; Ma, E. Tensile Ductility and Necking of Metallic Glass. *Nat. Mater.* **2007**, *6*, 735−739.

(16) Tian, L.; Cheng, Y. Q.; Shan, Z. W.; Li, J.; Wang, C. C.; Han, X. D.; Sun, J.; Ma, E. Approaching the Ideal Elastic Limit of Metallic Glasses. *Nat. Commun.* **2012**, *3*, 609.

(17) Wu, G.; Chan, K.-C.; Zhu, L. L.; Sun, L. G.; Lu, J. Dual-Phase Nanostructuring as a Route to High-Strength Magnesium Alloys. *Nature* **2017**, *545*, 80−83.

(18) Narayanan, S.; Cheng, G. M.; Zeng, Z.; Zhu, Y.; Zhu, T. Strain Hardening and Size Effect in Five-Fold Twinned Ag Nanowires. *Nano Lett.* **2015**, *15*, 4037−4044.

(19) Yue, Y. H.; Zhang, Q.; Zhang, X. J.; Yang, Z. Y.; Yin, P. G.; Guo, L. *In Situ* Observation of Twin Boundary Sliding in Single Crystalline Cu Nanowires. *Small* **2017**, *13*, 1604296.

(20) Yue, Y. H.; Liu, P.; Zhang, Z.; Han, X. D.; Ma, E. Approaching the Theoretical Elastic Strain Limit in Copper Nanowires. *Nano Lett.* **2011**, *11*, 3151−3155.

(21) Schiotz, J.; Jacobsen, K. W. A Maximum in the Strength of Nanocrystalline Copper. *Science* **2003**, *301*, 1357−1359.

DOI: 10.1021/acsnano.8b09195
ACS Nano 2019, 13, 4191−4198

(22) Liu, H. L.; Gong, Q. H.; Yue, Y. H.; Guo, L.; Wang, X. *Sub*-1 nm Nanowire Based Superlattice Showing High Strength and Low Modulus. *J. Am. Chem. Soc.* **2017**, *139*, 8579−8585.
(23) Puschmann, D.; Wolfart, S.; Ludwig, K.; Kern, M. Load-Bearing Capacity of All-Ceramic Posterior Inlay-Retained Fixed Dental Prostheses. *Eur. J. Oral Sci.* **2009**, *117*, 312−318.
(24) Garvie, R. C.; Hannink, R. H.; Pascoe, R. T. Ceramic Steel? *Nature* **1975**, *258*, 703−704.
(25) Tsukama, K.; Shimada, M. Thermal Stability of Y_2O_3 -Partially Stabilized Zirconia (Y-PSZ) and Y-PSZ/Al_2O_3 Composites. *J. Mater. Sci. Lett.* **1985**, *4*, 857−861.
(26) Garvie, R. C. The Occurrence of Metastable Tetragonal Zirconia as a Crystallite Size Effect. *J. Phys. Chem.* **1965**, *69*, 1238−1243.
(27) Hays, C. C.; Kim, C. P.; Johnson, W. L. Microstructure Controlled Shear Band Pattern Formation and Enhanced Plasticity of Bulk Metallic Glasses Containing *in situ* Formed Ductile Phase Dendrite Dispersions. *Phys. Rev. Lett.* **2000**, *84*, 2901−2904.
(28) Chen, H.; He, Y.; Shiflet, G. J.; Poon, S. J. Deformation-Induced Nanocrystal Formation in Shear Bands of Amorphous Alloys. *Nature* **1994**, *367*, 541−543.
(29) Tan, Z.; Wang, L.; Xue, Y. F.; Cheng, X. W. Strength-Improved $Al_{65}Cu_{16.5}Ti_{18.5}$ Amorphous/Crystalline Alloy Synthesized by Spark Plasma Sintering. *Mater. Sci. Eng., A* **2015**, *642*, 377−380.
(30) Zheng, K.; Wang, C. C.; Cheng, Y. Q.; Yue, Y. H.; Han, X. D.; Zhang, Z.; Shan, Z. W.; Mao, S. X.; Ye, M. M.; Yin, Y. D.; Ma, E. Electron-Beam-Assisted Superplastic Shaping of Nanoscale Amorphous Silica. *Nat. Commun.* **2010**, *1*, 1−8.
(31) Xi, X. K.; Zhao, D. Q.; Pan, M. X.; Wang, W. H.; Wu, Y.; Lewandowski, J. J. Fracture of Brittle Metallic Glasses: Brittleness or Plasticity. *Phys. Rev. Lett.* **2005**, *94*, 125510.
(32) Argon, A. S. Plastic Deformation in Metallic Glasses. *Acta Metall.* **1979**, *27*, 47−58.
(33) Zhang, Y. Y.; Li, Y. C.; Ming, P.; Zhang, Q.; Liu, T. X.; Jiang, L.; Cheng, Q. F. Ultrastrong Bioinspired Graphene-Based Fibers *via* Synergistic Toughening. *Adv. Mater.* **2016**, *28*, 2834−2839.
(34) Sun, J. K.; Li, Y. H.; Peng, Q. Y.; Hou, S. C.; Zou, D. C.; Shang, Y. Y.; Li, Y. B.; Li, P. X.; Du, Q. J.; Wang, Z. H.; Xia, Y. Z.; Xia, L. H.; Li, X. L.; Cao, A. Y. Macroscopic, Flexible, High-Performance Graphene Ribbons. *ACS Nano* **2013**, *7*, 10225−10232.
(35) Zhao, X. L.; Xu, Z.; Zheng, B. N.; Gao, C. Macroscopic Assembled, Ultrastrong and H_2SO_4-Resistant Fibres of Polymer-Grafted Graphene Oxide. *Sci. Rep.* **2013**, *3*, 3164.
(36) Jalili, R.; Aboutalebi, S. H.; Esrafilzadeh, D.; Shepherd, R. L.; Chen, J.; Aminorroaya-Yamini, S.; Konstantinov, K.; Minett, A. I.; Razal, J. M.; Wallace, G. G. Scalable One-Step Wet-Spinning of Graphene Fibers and Yarns from Liquid Crystalline Dispersions of Graphene Oxide: Towards Multifunctional Textiles. *Adv. Funct. Mater.* **2013**, *23*, 5344−5344.
(37) Han, Y. Q.; Lin, C. F.; Han, X. X.; Chang, Y. P.; Guo, C. H.; Jiang, F. C. Fabrication, Interfacial Characterization and Mechanical Properties of Continuous Al_2O_3 Ceramic Fiber Reinforced Ti/Al_3Ti Metal-Intermetallic Laminated (CCFR-MIL) Composite. *Mater. Sci. Eng., A* **2017**, *688*, 338−345.
(38) Li, R. G.; Nie, J. F.; Huang, G. J.; Xin, Y. C.; Liu, Q. Development of High-Strength Magnesium Alloys *via* Combined Processes of Extrusion, Rolling and Ageing. *Scr. Mater.* **2011**, *64*, 950−953.
(39) Anyanwu, I. A.; Kamado, S.; Kojima, Y. Aging Characteristics and High Temperature Tensile Properties of Mg-Gd-Y-Zr Alloys. *Mater. Trans.* **2001**, *42*, 1206−1211.
(40) Qiao, J. W.; Zhang, Y.; Feng, P.; Zhang, Q. M.; Chen, G. L. Strain Rate Response of Mechanical Behaviors for a Zr-Based Bulk Metallic Glass Matrix Composite. *Mater. Sci. Eng., A* **2009**, *515*, 141−145.
(41) Szuecs, F.; Kim, C. P.; Johnson, W. L. Mechanical Properties of $Zr_{56.2}Ti_{13.8}Nb_{5.0}Cu_{6.9}Ni_{5.6}Be_{12.5}$ Ductile Phase Reinforced Bulk Metallic Glass Composite. *Acta Mater.* **2001**, *49*, 1507−1513.
(42) Wu, F. F.; Zhang, Z. F.; Mao, S. X.; Peker, A.; Eckert, J. Effect of Annealing on the Mechanical Properties and Fracture Mechanisms of a $Zr_{56.2}Ti_{13.8}Nb_{5.0}Cu_{6.9}Ni_{5.6}Be_{12.5}$ Bulk-Metallic-Glass Composite. *Phys. Rev. B* **2007**, *75*, 88−92.

DOI: 10.1021/acsnano.8b09195
ACS Nano 2019, 13, 4191−4198